Non-noble-metallic Ni$_2$P nanoparticles modified O$_V$-BiOBr with boosting photoelectrochemical hydrogen evolution without sacrificial agent

Xibao Li [a,b,*], Yan Hu [a], Fan Dong [c], Juntong Huang [a], Lu Han [d,**], Fang Deng [b], Yidan Luo [a], Yu Xie [b], Chaozheng He [e,**], Zhijun Feng [a], Zhi Chen [a], Yongfa Zhu [f,**]

[a] School of Materials Science and Engineering, Nanchang Hangkong University, Nanchang 330063, China
[b] National-Local Joint Engineering Research Center of Heavy Metal Pollutants Control and Resource utilization, Nanchang Hangkong University, Nanchang 330063, China
[c] Institute of Fundamental and Frontier Sciences, University of Electronic Science and Technology of China, Chengdu 611731, China
[d] School of Materials and Metallurgy, University of Science and Technology Liaoning, Anshan 114051, China
[e] Institute of Environmental and Energy Catalysis, School of Materials Science and Chemical Engineering, Xi'an Technological University, Xi'an, Shaanxi 710021, China
[f] Department of Chemistry, Tsinghua University, Beijing 100084, China

ARTICLE INFO

ABSTRACT

Non-noble-metallic Ni$_2$P modified BiOBr with oxygen vacancy (O$_V$) was synthesized by solvothermal method to construct novel O$_V$-BiOBr/Ni$_2$P nanoheterojunction. Compared with O$_V$-BiOBr, the photoelectrochemical hydrogen evolution of O$_V$-BiOBr/Ni$_2$P was significantly improved. O$_V$-BiOBr/Ni$_2$P-2% showed the best hydrogen evolution rate of 455.34 μmol·cm^{-2}·h^{-1} without sacrificial agent, which was 5.94 times that of O$_V$-BiOBr and 12.88 times that of pristine BiOBr. It was found that an appropriate amount of Ni$_2$P loading enabled the closely contacted O$_V$-BiOBr/Ni$_2$P to have an optimal O$_V$ concentration, which realized the rapid electron-hole separation, simultaneously, the successful loading of Ni$_2$P can effectively enhance the light absorption capacity. The formation of Bi-O-P chemical bond and nanoheterojunctions jointly promote electron transfer and inhibit carrier recombination. Density functional theory (DFT) calculations find that the hydrogen adsorption free energy of O$_V$-BiOBr/Ni$_2$P heterojunction is the lowest in this system. This study will provide some guidance for efficient photoelectrochemical hydrogen evolution without sacrificial agent.

1. Introduction

Energy shortage, serious environmental pollution and natural disasters such as global warming and extreme weather changes frequently occur in recent years. The solar-driven photoelectrochemical (PEC) technology is considered to be ideal environmental pollution control and clean energy production technology, which is essential to promote the adjustment of energy structure driven by "carbon peaking and carbon neutrality" [1–3]. Among these, hydrogen energy has received significant attention as a clean (only water as a combustion product), high energy density (140 MJ·Kg^{-1}) and renewable energy source [3–5]. Since 1972, following pioneering work by Fujishima and Honda to discover that hydrogen could be produced by water splitting under ultraviolet light using TiO$_2$ as an electrode, PEC water splitting to generate hydrogen has been supposed as one of the technologies that can effectively solve the energy problem [6]. Recently, nurmeous semiconductor materials with satisfactory hydrogen evolution effect have aroused public attention, especially metal oxides, metal sulfides, metal nitrides, and non-metal semiconductors, which can be used as photoelectrodes for hydrogen evolution reaction [7–9]. Unfortunately, most of these materials can only perform limited effect in their practical applications due to their low carrier separation efficiency and poor stability.

In recent years, bismuth bromide oxide (BiOBr), whice has aroused public attention in the field of photocatalysis, is a typical layered material consisting of [Bi$_2$O$_2$]$^{2+}$ units interspersed with double [Br]$^-$ atomic sheets by van der Waals forces [10]. The presence of a built-in electric field between the layers that make up BiOBr is thought to facilitate the photogenerated carriers separation and transfer, moreover, it is widely used for CO$_2$ reduction, nitrogen fixation and degradation of organic

---

pollutants [11]. However, BiOBr has major limitations in the field of hydrogen production from water splitting owing to its wide optical band gap (2.6–2.9 eV) and fast carrier combination [12]. The doping, construction of heterojunctions, and introduction of defects have been considered as effective strategies to increase the carrier transport rate [13–17]. Feng et al. reported BiOBr/C Schottky junction composites by chemical vapor deposition (CVD) method, in which the BiOBr/C Schottky junction parallel junction has the highest hydrogen evolution rate, which can reach 2850 $\mu mol \cdot g^{-1} \cdot h^{-1}$, while the evolution rate of pristine BiOBr was almost zero, and this remarkable improvement in performance is attributed to the successful structure of the Schottky junction that boosts the rapid separation of charge carriers [18]. In addition, oxygen vacancy (O_V) is extensively applied in the generation of hydrogen by water splitting due to its effectiveness in intensifying the photon absorbance and reducing the activation energy of the reaction [19]. Shen et al. successfully introduced O_V into TiO_2 by N_2 treatment and exhibited a charge injection efficiency of 94.6% at 1.23 V vs. RHE due to the presence of O_V enhancing its light absorption, increasing the carrier density in TiO_2, promoting charge separation and the fact that O_V can reduce the overpotential of water oxidation by lowering the reaction activation energy, thus showing a better PEC charge injection efficiency [19]. Introducing oxygen vacancies (OVs) on the catalyst BiOBr has been considered a significant method to improve its performances. Tong et al. prepared ultrathin BiOBr nanosheets with rich surface OVs. Most of the OVs exposed on the surfaces which act as exposed catalytic site. For the photo-oxidation reaction of secondary amines, under the conditions of visible light, ambient temperature and atmosphere, the BiOBr nanosheets with rich surface OVs provided double conversion rate, 99% high selectivity and high stability compared to those with low O_V concentration [20]. Dong et al. confirmed that OVs can induce the formation of an intermediate level in the band structure of BiOBr and promote O_2 activation, thus producing $\cdot O_2^-$ species. Due to the synergistic effects of Bi metal and OVs, Bi metal@defective BiOBr showed highly enhanced visible light photocatalytic performance for NO removal [21].

Strategies to improve PEC performance usually include microstructure modulation, construction of heterostructured catalysts, introduction of chemical defects, and loading of cocatalysts. ZnO/V_2O_5 core-shell hetero-nanostructure was prepared by Hou et al. The core-shell structure ZnO/V_2O_5-600 with appropriate thickness of V_2O_5 layer has the extremely high carriers density, largest electrochemically active surface area, lowest charge recombination rate, and extended electron-hole lifetime by reason of the formation of the staggered gap junctions [22]. Yang et al. designed a new PEC water oxidation system, that inserting MXene nanosheets (MNs) between α-Fe_2O_3 and OEC. MNs act as the hole transfer mediators to efficiently suppress the interfacial charge recombination owing to the high hole mobility of MNs and the formation of built-in electric field at the MNs/α-Fe_2O_3 junction. The optimized photoanode of Co-Pi/MNs/α-Fe_2O_3 has remarkable photocurrent density [23]. Li et al. fabricated Ov-BiOBr/Cu_{2-x}S high-low junction composites with double defects (Ov and Cu vacancy). Since Ov acts as an electron capture center, Cu vacancy can act as a hole transport channel, which promotes carrier separation and greatly accelerates the carrier transport, significantly improving the PEC hydrogen evolution activity [24]. For pure In_2O_3, it exhibits low hole transfer ability under the function of visible light and bias voltage. Li et al. constructed the Z-scheme photoanode Ti-Fe_2O_3/In_2O_3 with rational energy band structure. The charge carrier migration is driven by the built-in electric field of the Z-scheme Ti-Fe_2O_3/In_2O_3 heterojunction [25]. To date, a number of noble metal-free cocatalysts have been discussed in details, like carbides, nitrides, sulfides, phosphides and multicomponent cocatalysts [26–29]. Due to the loading of CoP efficiently inhibiting the interfacial charge recombination, Du et al. utilized CoP nanoparticles for the surface modification of $BiVO_4$, which achieved excellent PEC performance [29]. Zhu et al. employed three TMPs (Fe_2P, Co_2P and Ni_2P) as cocatalysts for sulfur doped g-C_3N_4 (S-CN) and the optimum cocatalyst was Ni_2P in comparison, which stemmed from the fact

that Ni_2P/S-CN had the most suitable H* adsorption as well as the lowest overpotential, thus exhibiting high-efficiency charge separation and hydrogen production activity [30].

Bi metal precipitated from BiOBr could act both as a charge transfer bridge and as a hot electron donor [21]. Ni_2P with metallic nature acts as an electron acceptor during the process of photocatalytic reaction to accept the photoinduced electrons in the CB of O_V-BiOBr [30]. Moreover, the experimental results demonstrated that an appropriate amount of Ni_2P can act as a better H^+ receptor to promote the reduction of H^+ to H_2 [30]. Therefore, the heterojunction of cocatalyst Ni_2P and O_V-BiOBr exhibits more effective charge separation and charge transfer performance, which will provide new possibilities of engineering the co-catalyst and provide catalytic active sites for efficient photoelectrochemical hydrogen production. However, there are few reports on introducing defects of appropriate concentration into heterojunctions, especially the PEC work of BiOBr/Ni_2P heterojunctions containing oxygen defects.

In this work, Ni_2P was loaded onto bismuth oxybromide with appropriate concentration of oxygen vacancy (O_V-BiOBr) using a two-step solvothermal method. O_V-BiOBr/Ni_2P nanoheterojunction with strong chemical interaction was successfully prepared. The unique crystal structure, morphology, optical and photoelectrochemical properties of O_V-BiOBr/Ni_2P have also been characterized in detail. Under visible light irradiation and the action of bias voltage, O_V-BiOBr/Ni_2P-2% exhibited the best hydrogen evolution rate. This is attributed to the reason that the introduction of O_V and the heterojunction formed by the successful loading of Ni_2P can effectively promote the separation and transfer of charges. The introduction of O_V with certain concentration can effectively promote the transport of carriers, the successful loading of Ni_2P can significantly improve the light absorption capacity, as well as the construction of O_V-BiOBr/Ni_2P nanoheterojunction provides more active sites for the hydrogen evolution reaction. The concentration of O_V can be regulated by Ni_2P content in O_V-BiOBr/Ni_2P. O_V-BiOBr/Ni_2P displayed boosting PEC hydrogen evolution without sacrificial agent. The hydrogen adsorption free energy and the differential charge density of O_V-BiOBr/Ni_2P were firstly investigated and discussed.

2. Experimental

2.1. Experimental section

O_V-BiOBr nanospheres, Ni_2P and O_V-BiOBr/Ni_2P composites were prepared by a solvothermal method. The preparation of O_V-BiOBr/Ni_2P composites are described in Scheme 1. The prepared nickel foam,
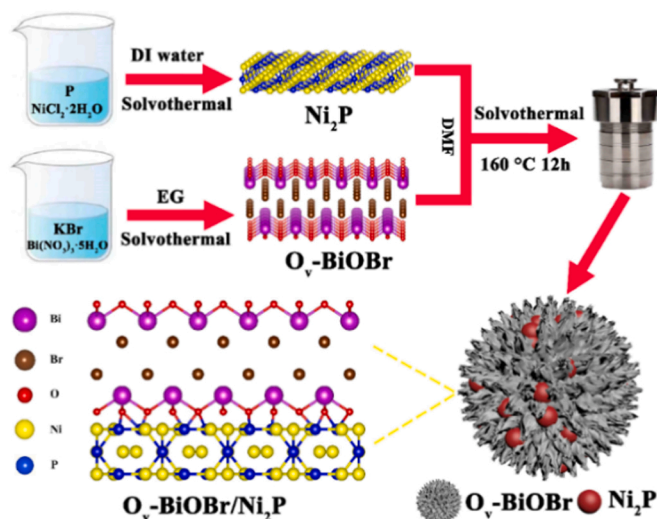
Scheme 1. The preparation process of O_V-BiOBr/Ni_2P.

saturated Ag/AgCl and Pt sheet electrode were used as the working electrode, reference electrode and counter electrode, respectively. Working electrodes were prepared by homogeneously loading the catalyst onto nickel foam. 1 M KOH (pH=13.6) and 0.5 M Na_2SO_4 (pH=7) were used for the electrolyte solution. Subsequently, the corresponding electrochemical tests were conducted. Detailed information about synthesis of catalysts (including BiOBr), characterizations, and photoelectrochemical measurements have been described in the section of supporting information.

2.2. Computational methods

All theoretical calculations were performed based on spin-polarized density functional theory route, which is described in detail in the section of supporting information.

3. Results and discussion

3.1. Morphology and structural characterization

As shown in Fig. 1(a)-(c), transmission electron microscopy (TEM) images display that Ni_2P is nanospheres with the average size of around 50 nm, which are dispersed uniformly on O_V-BiOBr nanospheres with a size of about 400 nm. The existence of Ni_2P as sufficient surface active

sites was verified. In addition, HRTEM images clearly show that the close connection between Ni_2P and O_V-BiOBr, and O_V-BiOBr/Ni_2P has obvious lattice fringes (Fig. 1(d)-(e)). The interplanar spacing of 0.277 nm and 0.221 nm corresponds to the (110) plane of BiOBr and the (111) plane of Ni_2P, respectively. In addition, lattice fringes with interplanar spacing of 0.332 nm are clearly observed, which are attributed to the (012) plane of Bi metal [31]. The corresponding element mapping images of O_V-BiOBr/Ni_2P are shown in Fig. 1(g)-(k), manifesting the presence of Bi, O, Br, Ni and P elements and the distribution of Ni_2P nanoparticles on the O_V-BiOBr nanospheres. To sum up, all characteristics indicate the successful synthesis of O_V-BiOBr/Ni_2P composites.

The X-ray diffraction (XRD) patterns shown in Fig. 2 demonstrate the crystal structure information of BiOBr, O_V-BiOBr, Ni_2P and O_V-BiOBr/Ni_2P. As indicated in the XRD pattern of Ni_2P, it was detected at approximately 40.68°, 44.52°, 47.34° and 54.19°, corresponding to the (111), (201), (210) and (300) planes of the hexagonal crystal system Ni_2P (PDF#03–0935). For O_V-BiOBr, the diffraction peaks at 27.06°, 37.88°, 39.67°, 44.51°, 48.68°, 56.00°, 59.37°, 62.09° and 64.34° correspond to the (012), (104), (110), (015), (202), (024), (107), (116), (122) planes of the hexagonal crystal system Bi (PDF#85–1329), which is the in-situ precipitation of some Bi from the BiOBr lattice [32]. However, no obvious Bi peak is found in the pristine BiOBr, indicating that the in-situ precipitation of Bi pure element can be formed only in
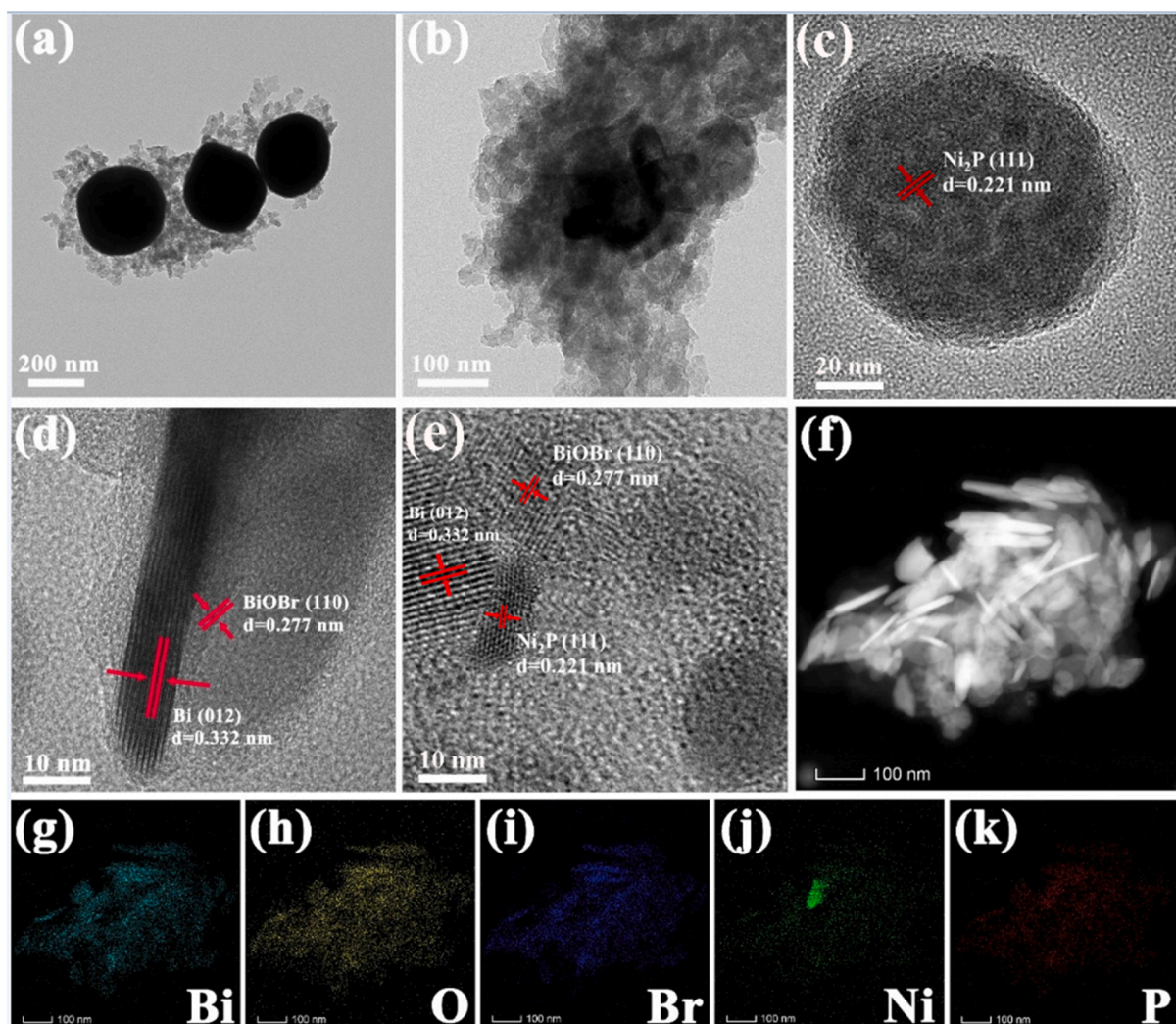
Fig. 1. (a)-(b) TEM images of O_V-BiOBr/Ni_2P, (c) TEM image of Ni_2P, (d)-(e) HRTEM images of O_V-BiOBr/Ni_2P, (g)-(k) element Bi, O, Br, Ni, P distribution in Fig. 1(f).
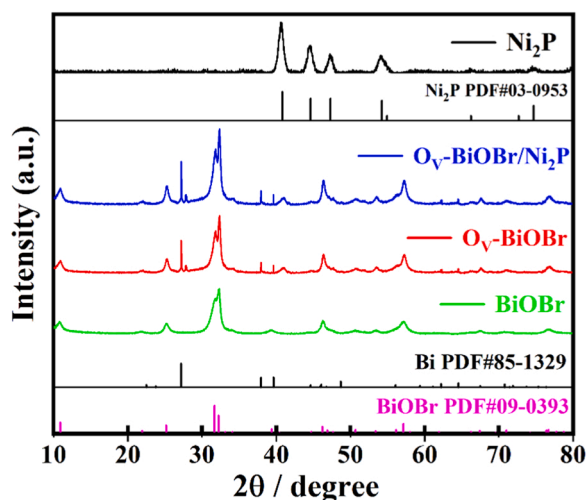
Fig. 2. XRD patterns of BiOBr, O_V-BiOBr, Ni_2P and O_V-BiOBr/Ni_2P.

O_V-BiOBr. For the O_V-BiOBr/Ni_2P composite material, it is difficult to observe the diffraction peaks of Ni_2P in the XRD pattern of O_V-BiOBr/-Ni_2P due to the micro-introduction of Ni_2P.

To verify the successful introduction of Ni_2P, in situ XPS technology was used to obtain the electron transfer direction at the heterojunction interface. The characteristic peaks of Bi, O, Br, Ni, P and C can be observed from Fig. 3(a), where the element C is the residual C of the instrument and the characteristic peaks of Ni and P are weak due to a small number of Ni_2P introduction. Fig. 3(b) displays the Bi 4 f profile of O_V-BiOBr/Ni_2P with two characteristic peaks observed at 159.0 eV and 164.3 eV attributing to Bi 4 $f_{7/2}$ and Bi 4 $f_{5/2}$ of Bi^{3+}, respectively. And the presence of two weaker characteristic peaks at 156.9 eV and 162.2 eV, which are attributed to Bi^0, again demonstrating the precipitation of Bi [33]. Similarly, as observed in Fig. 3(c) that the O 1 s can be fitted by characteristic peaks with binding energies of 528.7 eV, 530.7 eV and 532.5 eV, which is attributed to the Bi-O bond, O_V and the surface adsorbed -OH group, respectively [34]. Fig. 3(d) indicates that the characteristic peaks appearing at binding energies of 68.1 eV and 69.1 eV are associated with Br $3d_{5/2}$ and Br $3d_{3/2}$, respectively. For the

Ni 2p spectrum in Fig. 3(e), it can be divided into two parts, Ni $2p_{3/2}$ and Ni $2p_{1/2}$ energy level [35]. Among them, the characteristic peaks at Ni $2p_{1/2}$ at 880.0 eV, 874.4 eV and 869.3 eV are attributed to the satellite peaks, Ni(δ^+) species and Ni^{2+} of Ni_2P, separately. And the characteristic peaks at 861.3 eV, 856.2 eV and 852.5 eV located at Ni $2p_{3/2}$ correspond to the satellite peak, Ni(δ^+) species and Ni^{2+} of Ni_2P, separately [36]. The P 2p spectrum in Fig. 3(f) shows the appearance of two characteristic peaks at 130.4 eV and 133.6 eV, where the peak at 130.4 eV is attributed to the P(δ^-) of Ni_2P, which in combination with the conclusion of the Ni 2p spectrum proves the successful introduction of Ni_2P [37]. The peak of 133.6 eV is attributed to the oxide of P, which can be attributed to the formation of the Bi-O-P bond according to the reported literature [38]. However, compared with XPS under illumination, it can be found that the characteristic peaks in Bi 4 f, O 1 s, Br 3d, Ni 2p, and P 2p are obviously shifted, which is due to the change of the corresponding electron density. Among them, the binding energies of Bi, O and Br increase after illumination, which indicates that O_V-BiOBr loses electrons during the charge transport. Meanwhile, the binding energies of Ni and P decrease after illumination, thus Ni_2P gets electrons during charge transfer. Through the change of binding energy of each element, it can be obtained that the photogenerated electrons can be obtained from O_V-BiOBr to Ni_2P. To sum up, O_V-BiOBr and Ni_2P are combined through the chemical bond Bi-O-P bond, indicating that there is a strong chemical force between O_V-BiOBr and Ni_2P. And the successful detection of Bi^0, O_V as well as Ni_2P proves the successful synthesis of O_V-BiOBr/Ni_2P nanoheterojunction composites and the transfer of photogenerated electrons from O_V-BiOBr to Ni_2P.

Moreover, to investigate the influence of Ni_2P loading on the concentration of oxygen vacancy, electron paramagnetic resonance spectroscopy (EPR) was applied for analysis the samples BiOBr, O_V-BiOBr and O_V-BiOBr/Ni_2P with different Ni_2P loadings, as indicated in Fig. 4. Except for pure BiOBr, all the samples showed obvious signals at g = 2.002, and with increasing Ni_2P content, the peak strength of O_V decreased gradually, indicating that Ni_2P content can be very valid for regulating the concentration of O_V in the composites.

3.2. Photoelectrochemical properties

In order to assess the photoelectrochemical properties of the obtained materials under visible light, they were tested accordingly. As
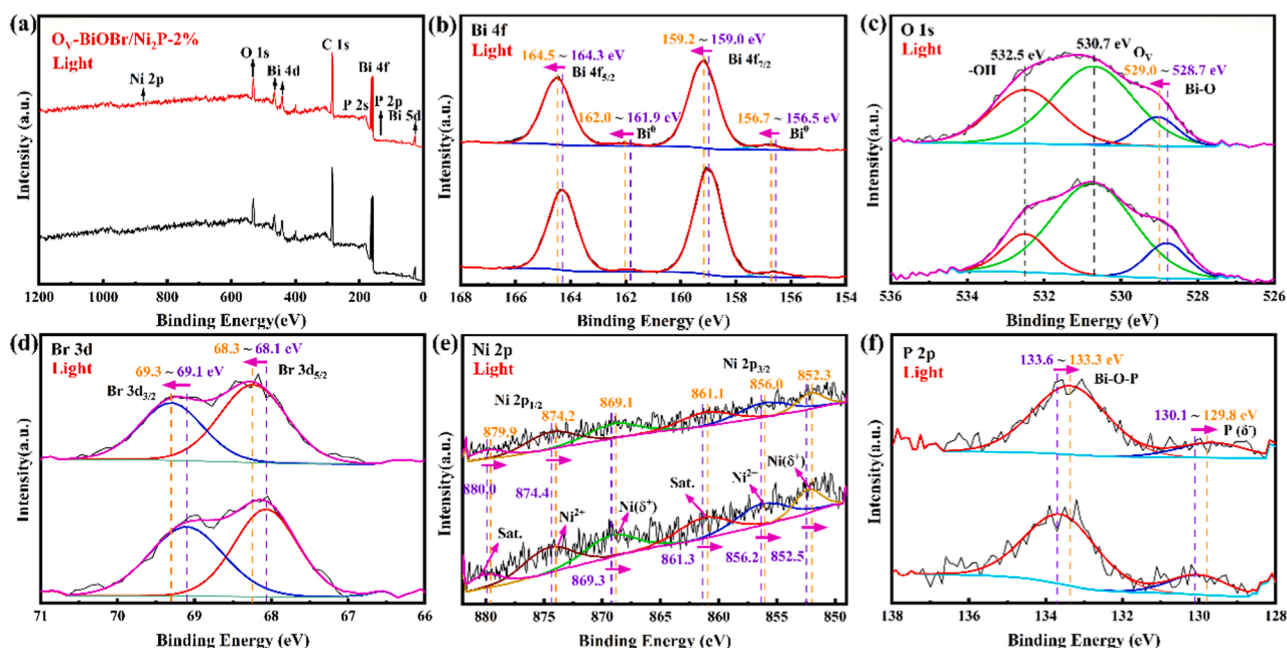

Fig. 3. In-situ XPS survey spectra of (a) full-spectrum, (b) Bi 4 f, (c) O 1 s, (d) Br, (e) Ni 2p and (f) P 2p of O_V-BiOBr/Ni_2P composites.
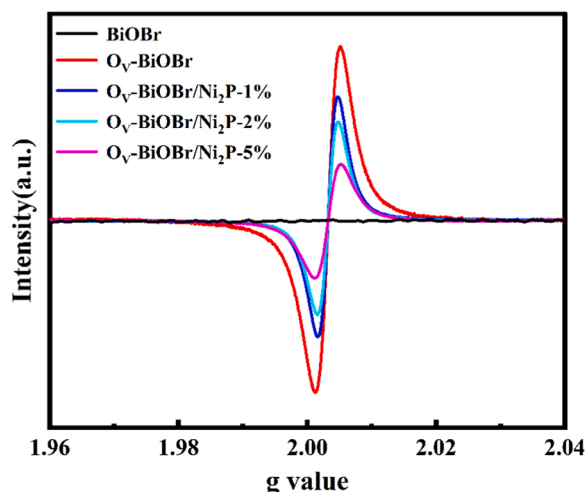
Fig. 4. EPR spectrum of BiOBr, O_V-BiOBr and O_V-BiOBr/Ni$_2$P with different contents.
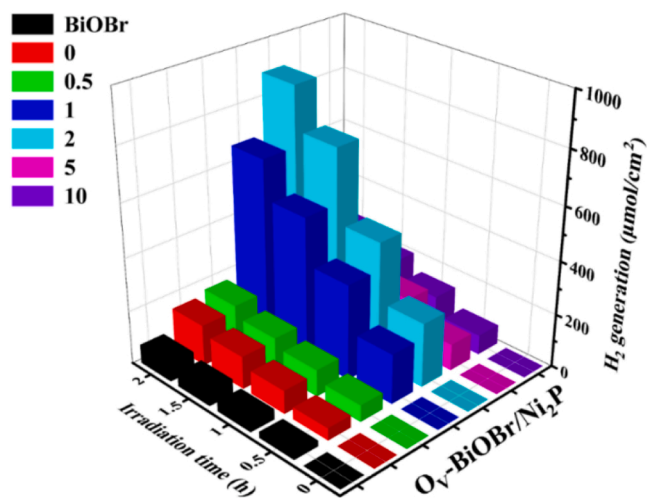

Fig. 6. Photoelectrochemical hydrogen evolution of O_V-BiOBr/Ni$_2$P composite samples with different Ni$_2$P contents under visible light irradiation.

indicated in Fig. 5, the hydrogen evolution reaction (HER) performance of the samples was tested under alkaline and neutral conditions using 1 M KOH and 0.5 M Na$_2$SO$_4$ as electrolyte solutions, respectively. As seen in Fig. 5(a), O_V-BiOBr/Ni$_2$P-2% shows the highest current density at the same potential. At the potential of -0.4 V vs. RHE, the current density of O_V-BiOBr/Ni$_2$P-2% can reach 82.86 mA·cm^{-2}, which is 2.82 times and 3.57 times that of O_V-BiOBr and BiOBr, respectively. To demonstrate the pervasiveness of the sample, the corresponding photoelectrochemical tests were performed in 0.5 M Na$_2$SO$_4$. Fig. 5(b) shows that O_V-BiOBr/Ni$_2$P-2% still has the maximum current density in the electrolyte solution at pH= 7, indicating that it has the strongest reduction activity and the optimal HER performance. The current density of O_V-BiOBr/Ni$_2$P shows an increasing and then decreasing trend with the increase of Ni$_2$P content in both experiments conducted under alkaline and neutral conditions, which indicates that the introduction of Ni$_2$P can enhance the reducing properties of O_V-BiOBr/Ni$_2$P with effect, but the excessive Ni$_2$P may become an electron trap, thus reducing the HER performance of O_V-BiOBr/Ni$_2$P.

In order to quantify the HER performance of the sample, 1 M KOH without any sacrificial agent was used as the electrolyte solution and a potential of -0.4 V vs. RHE was applied so that the corresponding photoelectrochemical hydrogen evolution experiments could be performed on the electrode under the effects of visible light and applied bias voltage. As shown in Fig. 6, BiOBr exhibits a low photoelectrochemical hydrogen evolution activity, generating only 71.26 μmol/cm^2 of hydrogen for 2 h. The introduction of O_v can produce 153.18 μmol/cm^2

of hydrogen, which is 2.15 times that of pristine BiOBr. This is attributed to the fact that a certain amount of O_v can effectively promote charge transfer and improve hydrogen production performance. The PEC hydrogen evolution activity of the O_V-BiOBr/Ni$_2$P electrodes was significantly enhanced after the introduction of Ni$_2$P. Among them, O_V-BiOBr/Ni$_2$P-2% showed the highest PEC hydrogen evolution activity, and the hydrogen evolution amount in 2 h could reach 891.96 μmol/cm^2, which was 5.82 and 12.52 times that of O_V-BiOBr and BiOBr, respectively. This is because the formation of heterojunction between O_V-BiOBr and Ni$_2$P can promote the transport of carriers. Fig. 7(a) illustrates the PEC hydrogen evolution rates of the BiOBr and O_V-BiOBr/Ni$_2$P electrodes with different Ni$_2$P contents. In agreement with the hydrogen evolution yield results, O_V-BiOBr/Ni$_2$P-2% shows supreme hydrogen evolution rate of 455.34 μmol·cm^{-2}·h^{-1}, which is 5.94 and 12.88 times that of O_V-BiOBr and BiOBr, respectively. The PEC hydrogen evolution rates are compared with those of Bi-based materials reported in the literature, as shown in Table 1. The results indicate that O_V-BiOBr/Ni$_2$P has the great performance in PEC hydrogen evolution. The hydrogen evolution activity of O_V-BiOBr/Ni$_2$P electrode decreases with the increase of Ni$_2$P content. The reason may be that excess Ni$_2$P may not be closely combined with O_V-BiOBr, which causes problems in the bonding of heterojunction interface, thus reducing the hydrogen evolution activity of the electrode. In addition, high Ni$_2$P loading will increase the particle size of the cocatalyst, which will weaken its surface effect and affect its catalytic performance [39]. Therefore, a suitable Ni$_2$P loading is important. The stability of PEC hydrogen precipitation
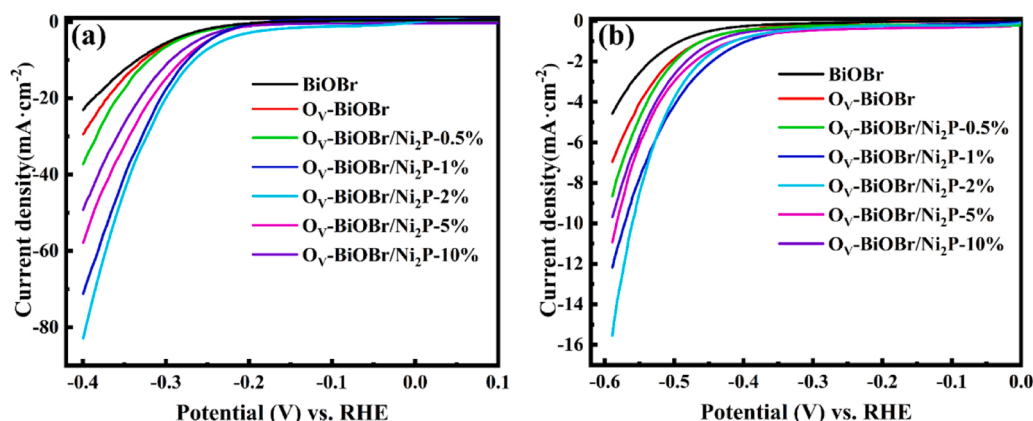

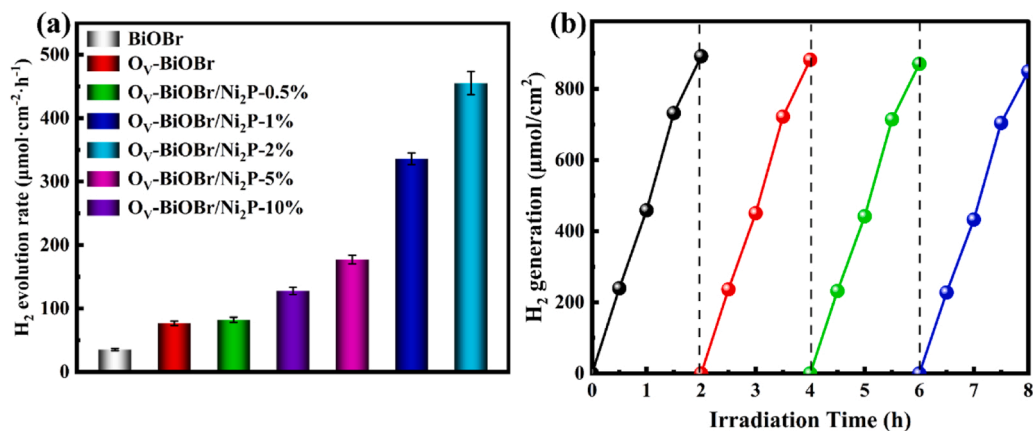**Fig. 5.** HER performance of sample in (a) 1 M KOH (pH=13.6) and (b) 0.5 M Na$_2$SO$_4$ (pH=7).

Fig. 7. (a) Hydrogen evolution rate of different samples, (b) hydrogen evolution cycle test of O_V-BiOBr/Ni$_2$P-2%.

Table 1
Comparison of the hydrogen evolution rate between the prepared sample and the published catalysts.

Catalyst	Electrolyte	H$_2$ evolution rate (μmol·cm^2·h^{-1})	Ref.
O_V-BiOBr/Ni$_2$P	1 M KOH	455.34	This work
Bi$_2$S$_3$/BiVO$_4$	0.1 M Na$_2$S+ 0.02 M Na$_2$SO$_3$	417	[40]
Bi$_2$O$_3$/Al$_2$Bi$_{24}$O$_{39}$/ Al$_2$Bi$_{48}$O$_{75}$	0.5 M Na$_2$SO$_4$	348	[41]
Bi/Bi$_2$MoO$_6$/TiO$_2$	0.2 M Na$_2$SO$_4$	173.41	[42]
BiVO$_4$ @Fe$_2$O$_3$	12.5 mL lactic acid+ 2.5 mL H$_2$PtCl$_6$·6 H$_2$O+ 82.5 mL DI water	139.0	[43]
Bi$_{0.9}$Gd$_{0.1}$Fe$_{0.75}$Co$_{0.25}$O$_3$	1 M NaOH	74.57	[44]
NiFe-MOFs/BiVO$_4$	0.5 M K$_3$BO$_3$	68.1	[45]
BiVO$_4$	0.5 M Na$_2$SO$_4$	34.44	[46]
Bi$_2$S$_3$-BiOBr/TiO$_2$	0.25 M Na$_2$S+ 0.35 M Na$_2$SO$_3$	17.26	[47]

was tested for O_V-BiOBr/Ni$_2$P-2%, as indicated in Fig. 7(b). After four cycles of PEC hydrogen evolution experiments, the hydrogen production of O_V-BiOBr/Ni$_2$P-2% displays negligible reduction, illustrating that O_V-BiOBr/Ni$_2$P has eminent stability for photoelectrochemical catalytic hydrogen production.

3.3. Photoelectrochemical mechanism analysis

The photoabsorption ability is one of the important considerations influencing the photoelectrochemical properties of semiconductor materials, therefore the UV-Vis diffuse absorption spectra (UV-Vis DRS) of the materials were tested, as indicated in Fig. 8(a)-(b). Compared with BiOBr, O_V-BiOBr and all the O_V-BiOBr/Ni$_2$P composites show significant light absorption enhancement in the near-infrared region, which proves that the introduction of oxygen vacancy can strengthen the light absorption ability of the semiconductor. The absorption edge of the O_V-BiOBr/Ni$_2$P composites did not shift significantly after loading Ni$_2$P, which is related to the metallic nature exhibited by Ni$_2$P [48]. The band gaps of O_V-BiOBr and BiOBr were attained by the calculation of Tauc's
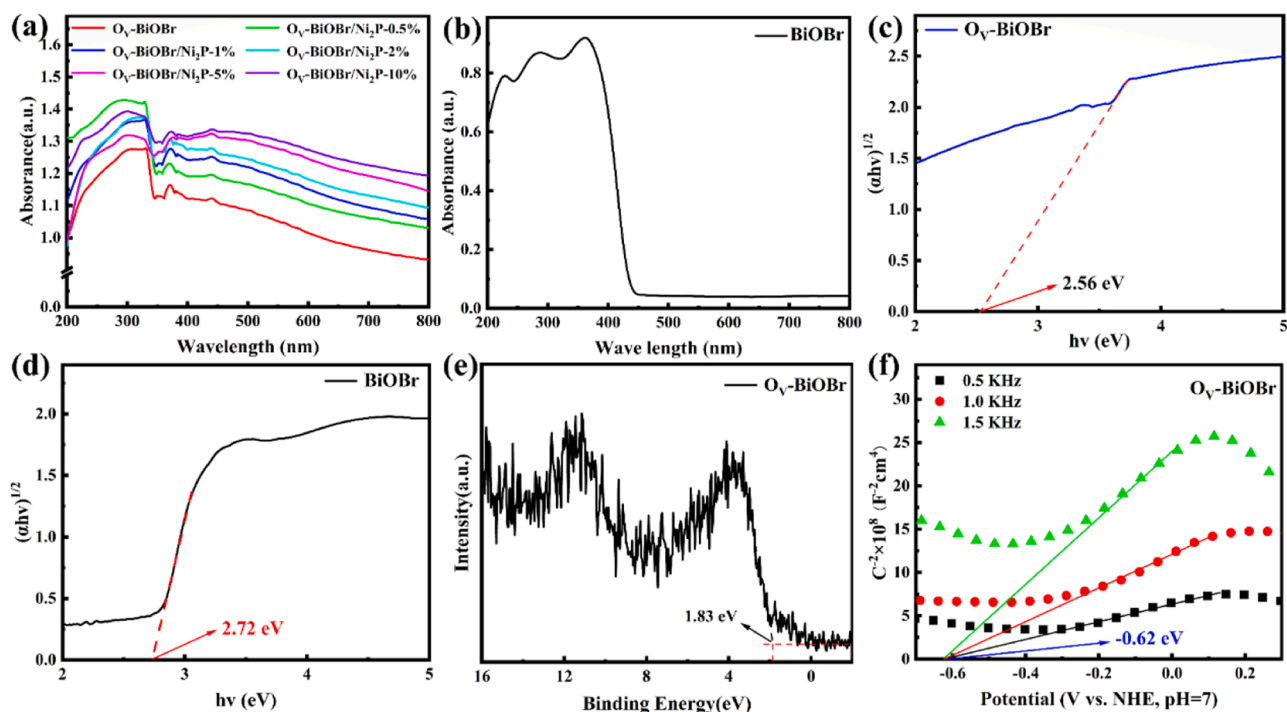

Fig. 8. UV-Vis DRS curves of (a) O_V-BiOBr/Ni$_2$P and (b) BiOBr, calculated band gaps of (c) O_V-BiOBr and (d) BiOBr, (e) VB-XPS and (f) MS curves of O_V-BiOBr.

formula [49]. Fig. 8(c)-(d) show that the introduction of oxygen vacancies reduces the band gap of the semiconductor from 2.72 eV to 2.56 eV. The valence band (VB) of O_V-BiOBr was also tested using VB-XPS, which can be calculated using Eq. (1):

$$E_{NHE} = \varphi + E_{VB-XPS} - 4.44 \qquad (1)$$

where E_{NHE} is the standard hydrogen potential and φ is the instrumental work function (4.55 eV) [50]. As a consequence, the VB of O_V-BiOBr can be obtained as 1.94 eV (Fig. 8e). The flat-band potential of O_V-BiOBr can be detected by the Mott-Schottky (MS) curves. As depicted in Fig. 8(f), the conduction band (CB) of O_V-BiOBr is − 0.62 eV and O_V-BiOBr is an n-type semiconductor (the slope of the curve is positive) [51].

To further explore the separation and transport of photogenerated carriers, the corresponding photoelectrochemical tests were performed on the samples. As seen in Fig. 9(a), under visible light illumination, O_V-BiOBr/Ni₂P-2% shows the maximum photocurrent density of 43.92 $\mu A \cdot cm^{-2}$, which is 4.15 and 9.04 times that of O_V-BiOBr and BiOBr, respectively. The excessive Ni₂P loading leads to the weakening of the photocurrent, a phenomenon that is in extremely consistent with the hydrogen evolution performance of O_V-BiOBr/Ni₂P. This again proves that the oxygen vacancy and the introduction of an appropriate amount of Ni₂P is favourable to the separation of photogenerated carriers. Furthermore, the transport properties of carriers were characterized by electrochemical impedance spectroscopy (EIS), as depicted in Fig. 9(b). Compared with O_V-BiOBr and BiOBr, O_V-BiOBr/Ni₂P shows a smaller semicircular arc, indicating its superior charge characteristics. And the transfer resistance of each sample was calculated by simulation circuit simulation, where Rs, Rif, Rct, CPE1 and CPE2 represent the solution resistance, interfacial charge transfer resistance, carrier migration resistance and Constant Phase Element 1 and 2, respectively. The calculation results of transfer resistance are shown in Table 2. The transfer resistance of O_V-BiOBr/Ni₂P-2% is the smallest with only 2444 ohm, indicating that O_V-BiOBr/Ni₂P-2% has excellent carrier migration performance.

In addition, to investigate the charge transfer process of O_V-BiOBr/Ni₂P, O_V-BiOBr, Ni₂P and O_V-BiOBr/Ni₂P were detected using VB-XPS, and the corresponding work function (Φ) was calculated by the following formula:[50,52].

$$\Delta V = \Delta\Phi - \varphi \qquad (2)$$

where ΔV is the contact potential difference, which represents the distance between the two inflection points (IP) of the curve, φ is the work function of the instrument with a value of 4.55 eV. As illustrated in Fig. 10(a)-(c), the work functions of O_V-BiOBr, Ni₂P and O_V-BiOBr/Ni₂P can be calculated to be 7.17, 6.09 and 6.63 eV, respectively. When O_V-BiOBr and Ni₂P are in close contact, the electrons will be transferred

**Table 2**
Resistance simulation results of samples.

Samples	Rct (ohm)
BiOBr	24,261
O_V-BiOBr	17,329
O_V-BiOBr/Ni₂P-0.5%	5287
O_V-BiOBr/Ni₂P-1%	2863
O_V-BiOBr/Ni₂P-2%	2444
O_V-BiOBr/Ni₂P-5%	3008
O_V-BiOBr/Ni₂P-10%	3194

from Ni₂P to O_V-BiOBr because the Fermi energy level (E_f) of Ni₂P is higher than that of O_V-BiOBr, and the energy band of O_V-BiOBr also bends downward. An electron accumulation layer is formed on the surface of O_V-BiOBr because of electrons transfer. Similarly, an electron depletion layer is formed on the surface of Ni₂P, leading to the formation of an internal electric field (IEF) pointing from Ni₂P to O_V-BiOBr. Under light illumination, the IEF induces the transition of photogenerated electrons from the CB of O_V-BiOBr to that of Ni₂P, which acts as a reaction active site and "electron collector" to accelerate the electron transfer and promote the reduction reaction [53].

To reveal the influences of O_V and heterojunction on the hydrogen evolution performance of the O_V-BiOBr/Ni₂P system, the corresponding density functional theory (DFT) calculations were conducted. Fig. 11(a) shows the H* adsorption free energies of BiOBr, O_V-BiOBr and O_V-BiOBr/Ni₂P, which are − 1.25 eV, − 0.73 eV and − 0.38 eV, respectively. It illustrates that the hydrogen adsorption free energy of O_V-BiOBr/Ni₂P heterojunction is the lowest, followed by O_V-BiOBr and BiOBr, respectively. This indicates that the order of hydrogen evolution activity is O_V-BiOBr/Ni₂P > O_V-BiOBr > BiOBr, which is agreement with the results of previous hydrogen evolution experiments. It demonstrates that the synergistic effect of Ni₂P and O_V facilitates the H* adsorption, making O_V-BiOBr/Ni₂P producing much more favourable H₂ evolution activity. From the EPR detection results, it can be concluded that the Ni₂P content can adjust the concentration of O_V in the composite, but when the concentration is too high, O_V will become a trapping center and lead to charge recombination. Therefore, a suitable Ni₂P content enables the closely contacted O_V-BiOBr/Ni₂P to have an optimal O_V concentration, which has more advantages and less drawbacks for its photoelectric performance. Therefore, the introduction of Ni₂P cocatalyst and the construction of O_V can more efficiently improve the hydrogen evolution performance of the catalysts. Simultaneously, to further clarify the hydrogen evolution mechanism of O_V-BiOBr/Ni₂P, the differential charge density of O_V-BiOBr/Ni₂P was investigated, as shown in Fig. 11(b). Due to the formation of heterojunction at the interface of O_V-BiOBr/Ni₂P, the transfer of electrons from Ni₂P to O_V-BiOBr is promoted, thus forming an IEF pointing from Ni₂P to O_V-BiOBr,
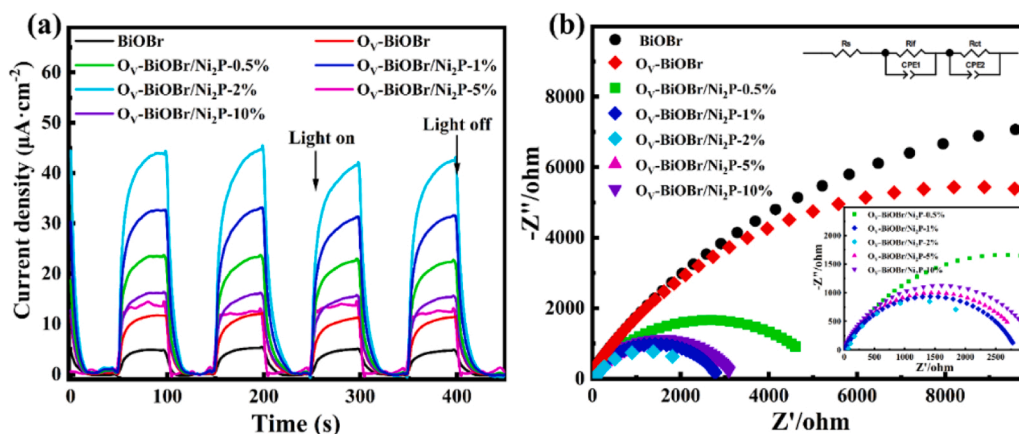
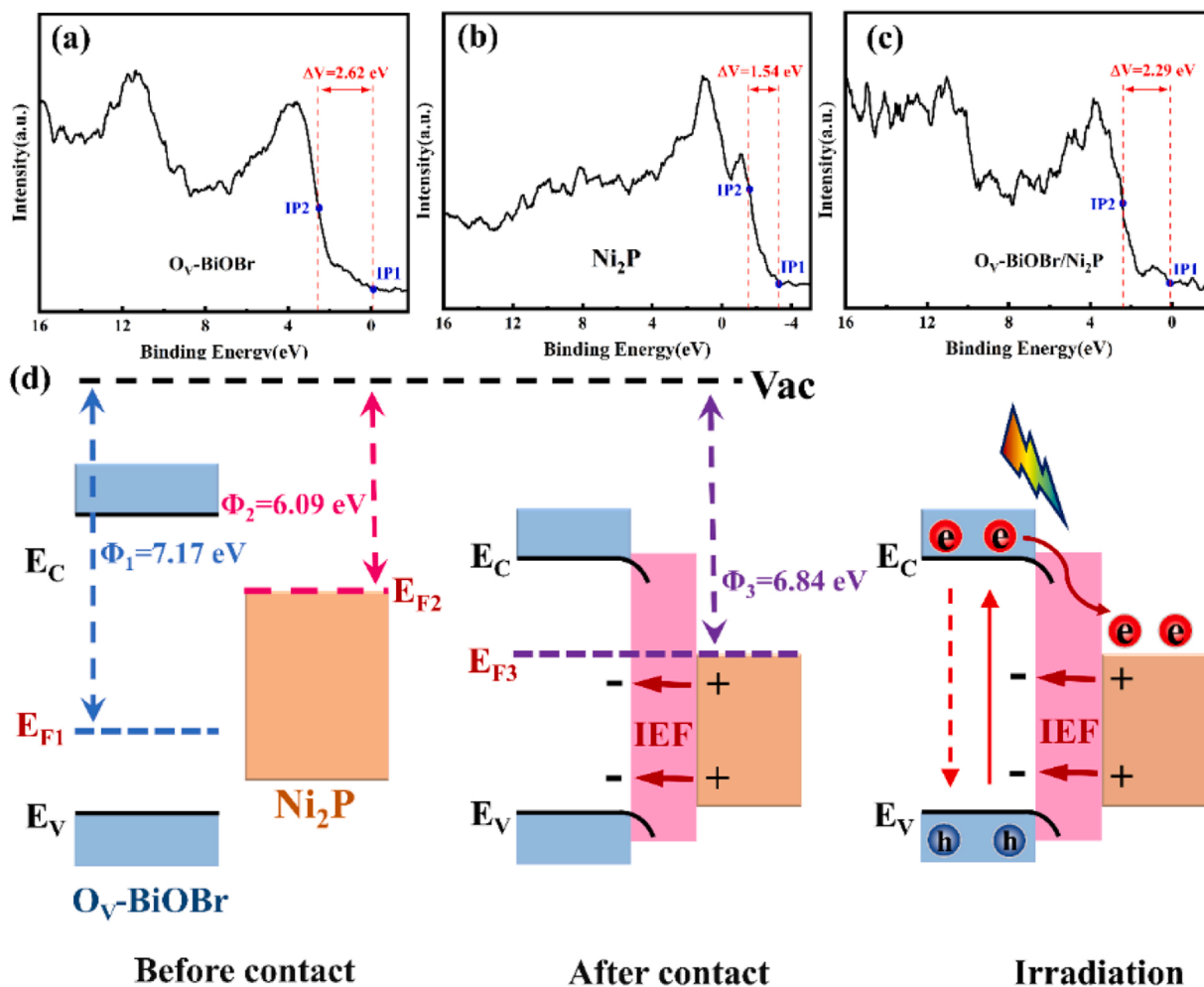**Fig. 9.** (a) Transient photocurrent and (b) EIS diagram of as-prepared samples.

Fig. 10. Work functions of (a) O_V-BiOBr, (b) Ni_2P and (c) O_V-BiOBr/Ni_2P; (d) Schematic diagram of the formation of IEF and electron transfer mechanism.
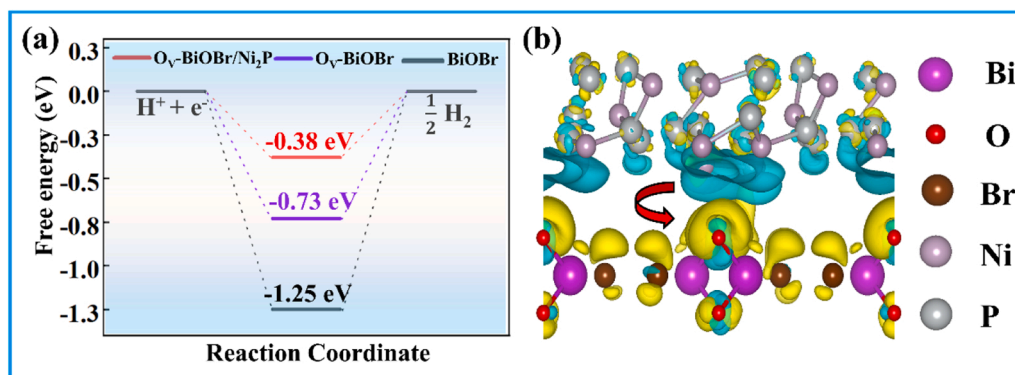

Fig. 11. (a) Free energy diagram of H* adsorption of BiOBr, O_V-BiOBr and O_V-BiOBr/Ni_2P at 0 V vs. RHE; (b) differential charge density of O_V-BiOBr/Ni_2P. Blue and yellow colors represent the charge losing and gaining, respectively.

which is more beneficial to the hydrogen evolution reaction.

Based on the above experimental and analytical results, the mechanism of O_V-BiOBr/Ni_2P photoelectrochemical hydrogen evolution is put forward, as indicated in Fig. 12. Due to the difference of Fermi energy level, the IEF is formed from Ni_2P pointing to O_V-BiOBr. Under light illumination, the IEF at the interface will accelerate the electron transfer from the CB of O_V-BiOBr to Ni_2P, and the formation of nano-heterojunction promotes the spatial separation of carriers. Due to the metal-like nature of Ni_2P cocatalyst, the transfer rate of electrons is

accelerated and allowed to move to the nickel foam electrode. Under the effect of applied bias voltage, the electrons on the nickel foam will be transferred to the counter electrode of Pt sheet with the external circuit and reduce H_2O to H_2 on the surface of Pt, while the photogenerated holes on the VB of O_V-BiOBr can oxidize H_2O to O_2 to realize PEC water splitting. Owing to the introduction of O_V and the synergistic effect of O_V-BiOBr/Ni_2P heterojunction, it can realize the rapid separation and more efficient transfer of electron-hole pairs, which exhibits highly efficient PEC hydrogen evolution activity without the addition of any
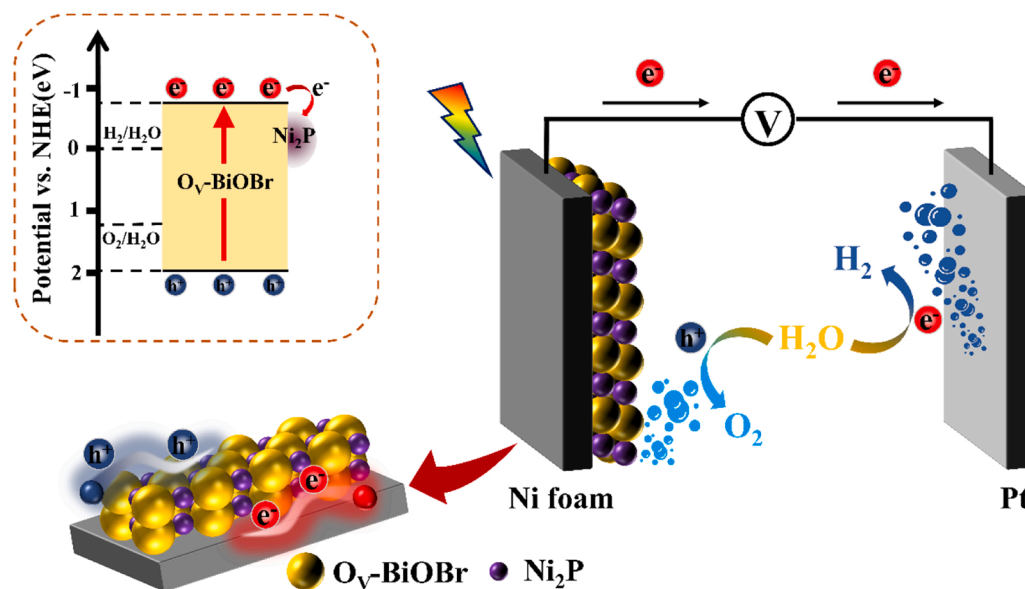
Fig. 12. Schematic diagram of PEC hydrogen evolution mechanism of O_V-BiOBr/Ni_2P.

sacrificial agent.

4. Conclusions

In summary, O_V-BiOBr/Ni_2P nanoheterojunction composites with excellent PEC hydrogen evolution performance were synthesized by a facile solvothermal method. There is a strong chemical interaction between O_V-BiOBr and Ni_2P, mainly through the formation of Bi-O-P chemical bond. Without adding of any sacrificial agent, O_V-BiOBr/Ni_2P-2% has supreme hydrogen evolution rate of 455.34 $\mu mol \cdot cm^{-2} \cdot h^{-1}$, which is 5.94 and 12.88 times that of O_VBiOBr and pristine BiOBr, respectively. This is because the introduction of O_V with certain concentration can effectively promote the carrier transport, and the successful loading of Ni_2P can evidently improve the light absorption capacity, as well as the construction of O_V-BiOBr/Ni_2P nanoheterojunction provides more active sites for the hydrogen evolution reaction. Moreover, both the carrier separation facilitated by the formation of the O_V-BiOBr/Ni_2P nanoheterojunction and the excellent electrical conductivity of the nickel foam accelerate the electron transport, allowing more electrons to participate in the hydrogen evolution reaction and exhibiting excellent PEC hydrogen evolution performance. This work will provide a theoretical and experimental basis for the research of hydrogen generation from PEC photoelectrode materials without sacrificial agent.

CRediT authorship contribution statement

Xibao Li: Supervision, Resources, Writing - Review & Editing, **Yan Hu:** Data curation, Writing- Original draft preparation, **Fan Dong:** Visualization, Writing - Review & Editing, **Juntong Huang:** Methodology, Data Curation, **Lu Han:** Validation, Data Curation, **Fang Deng:** Formal analysis, **Yidan Luo:** Investigation, **Yu Xie:** Formal analysis, **Chaozheng He:** Data Curation, **Zhijun Feng:** Formal analysis, **Zhi Chen:** Validation, **Yongfa Zhu:** Project administration, Resources, Conceptualization.

Declaration of Competing Interest

The authors declare that they have no known competing financial interests or personal relationships that could have appeared to influence the work reported in this paper.

Data Availability

Data will be made available on request.

Appendix A. Supporting information

Supplementary data associated with this article can be found in the online version at doi:10.1016/j.apcatb.2022.122341.

References

[1] S. Dong, Y. Zhao, J. Yang, X. Liu, W. Li, L. Zhang, Y. Wu, J. Sun, J. Feng, Y. Zhu, Visible-light responsive PDI/rGO composite film for the photothermal catalytic degradation of antibiotic wastewater and interfacial water evaporation, Appl. Catal. B Environ. 291 (2021) 120127.

[2] S. Bai, H. Qiu, M. Song, G. He, F. Wang, Y. Liu, L. Guo, Porous fixed-bed photoreactor for boosting C–C coupling in photocatalytic CO_2 reduction, eScience 2 (2022) 428–437.

[3] R. Liu, Z. Zheng, J. Spurgeon, X. Yang, Enhanced photoelectrochemical water-splitting performance of semiconductors by surface passivation layers, Energy Environ. Sci. 7 (2014) 2504–2517.

[4] Y. Li, F. Gong, Q. Zhou, X. Feng, J. Fan, Q. Xiang, Crystalline isotype heptazine-/triazine-based carbon nitride heterojunctions for an improved hydrogen evolution, Appl. Catal. B Environ. 268 (2020), 118381.

[5] X. Li, Q. Luo, L. Han, F. Deng, Y. Yang, F. Dong, Enhanced photocatalytic degradation and H_2 evolution performance of NCDs/S-C_3N_4 S-scheme heterojunction constructed by π-π conjugate self-assembly, J. Mater. Sci. Technol. 114 (2022) 222–232.

[6] A. Fujishima, K. Honda, Electrochemical photolysis of water at a semiconductor electrode, Nature 238 (1972) 37–38.

[7] X. Li, S. Liu, K. Fan, Z. Liu, B. Song, J. Yu, MOF-based transparent passivation layer modified ZnO nanorod arrays for enhanced photo-electrochemical water splitting, Adv. Energy Mater. 8 (2018), 1800101.

[8] S. Dong, L. Xia, X. Chen, L. Cui, W. Zhu, Z. Lu, J. Sun, M. Fan, Interfacial and electronic band structure optimization for the adsorption and visible-light photocatalytic activity of macroscopic $ZnSnO_3$/graphene aerogel, Compos. Part B Eng. 215 (2021), 108765.

[9] J. Fu, Z. Fan, M. Nakabayashi, H. Ju, N. Pastukhova, Y. Xiao, C. Feng, N. Shibata, K. Domen, Y. Li, Interface engineering of Ta$_3$N$_5$ thin film photoanode for highly efficient photoelectrochemical water splitting, Nat. Commun. 13 (2022) 729.

[10] M. Shi, G. Li, J. Li, X. Jin, X. Tao, B. Zeng, E.A. Pidko, R. Li, C. Li, Intrinsic facet-dependent reactivity of well-defined BiOBr nanosheets on photocatalytic water splitting, Angew. Chem. Int. Ed. 59 (2020) 6590–6595.

[11] H. Li, J. Shang, Z. Ai, L. Zhang, Efficient visible light nitrogen fixation with BiOBr nanosheets of oxygen vacancies on the exposed {001} facets, J. Am. Chem. Soc. 137 (2015) 6393–6399.

[12] Q. Chi, G. Zhu, D. Jia, W. Ye, Y. Wang, J. Wang, T. Tao, F. Xu, G. Jia, W. Li, P. Gao, Built-in electric field for photocatalytic overall water splitting through a TiO$_2$/BiOBr P–N heterojunction, Nanoscale 13 (2021) 4496–4504.

[13] X. Li, J. Zhang, Y. Huo, K. Dai, S. Li, S. Chen, Two-dimensional sulfur- and chlorine-codoped g-C$_3$N$_4$/CdSe-amine heterostructures nanocomposite with effective interfacial charge transfer and mechanism insight, Appl. Catal. B Environ. 280 (2021), 119452.

[14] S. Dong, L. Cui, Y. Tian, L. Xia, Y. Wu, J. Yu, D.M. Bagley, J. Sun, M. Fan, A novel and high-performance double Z-scheme photocatalyst ZnO-SnO$_2$-Zn$_2$SnO$_4$ for effective removal of the biological toxicity of antibiotics, J. Hazard. Mater. 399 (2020), 123017.

[15] Z. Jiang, Q. Chen, Q. Zheng, R. Shen, P. Zhang, X. Li, Constructing 1D/2D schottky-based heterojunctions between Mn$_{0.2}$Cd$_{0.8}$S nanorods and Ti$_3$C$_2$ nanosheets for boosted photocatalytic H$_2$ evolution, Acta Phys. Chim. Sin. 37 (2021), 2010059.

[16] S. Li, M. Cai, Y. Liu, C. Wang, K. Lv, X. Chen, S-scheme photocatalyst TaON/Bi$_2$WO$_6$ nanofibers with oxygen vacancies for efficient abatement of antibiotics and Cr(VI): Intermediate eco-toxicity analysis and mechanistic insights, Chin. J. Catal. 43 (2022) 2652–2664.

[17] X. Li, B. Kang, F. Dong, Z. Zhang, X. Luo, L. Han, J. Huang, Z. Feng, Z. Chen, J. Xu, B. Peng, Z.L. Wang, Enhanced photocatalytic degradation and H$_2$/H$_2$O$_2$ production performance of S-pCN/WO$_{2.72}$ S-scheme heterojunction with appropriate surface oxygen vacancies, Nano Energy 81 (2021).

[18] X. Zheng, L. Feng, Y. Dou, H. Guo, Y. Liang, G. Li, J. He, P. Liu, J. He, High carrier separation efficiency in morphology-controlled BiOBr/C schottky junctions for photocatalytic overall water splitting, ACS Nano 15 (2021) 13209–13219.

[19] X. Lv, L. Tao, M. Cao, X. Xiao, M. Wang, Y. Shen, Enhancing photoelectrochemical water oxidation efficiency via self-catalyzed oxygen evolution: A case study on TiO$_2$, Nano Energy 44 (2018) 411–418.

[20] X. Tong, X. Cao, T. Han, W.C. Cheong, R. Lin, Z. Chen, D. Wang, C. Chen, Q. Peng, Y. Li, Convenient fabrication of BiOBr ultrathin nanosheets with rich oxygen vacancies for photocatalytic selective oxidation of secondary amines, Nano Res. 12 (2019) 1625–1630.

[21] X. Dong, W. Zhang, Y. Sun, J. Li, W. Cen, Z. Cui, H. Huang, F. Dong, Visible-light-induced charge transfer pathway and photocatalysis mechanism on Bi semimetal@defective BiOBr hierarchical microspheres, J. Catal. 357 (2018) 41–50.

[22] T. Hou, M.A. Johar, R. Boppella, M.A. Hassan, S.J. Patil, S.W. Ryu, D. Lee, Vertically aligned one-dimensional ZnO/V$_2$O$_5$ core–shell hetero-nanostructure for photoelectrochemical water splitting, J. Energy Chem. 49 (2020) 262–274.

[23] G. Yang, S. Li, X. Wang, B. Ding, Y. Li, H. Lin, D. Tang, X. Ren, Q. Wang, S. Luo, J. Ye, A universal strategy boosting photoelectrochemical water oxidation by utilizing MXene nanosheets as hole transfer mediators, Appl. Catal. B Environ. 297 (2021) 120268.

[24] X. Li, Q. Liu, F. Deng, J. Huang, L. Han, C. He, Z. Chen, Y. Luo, Y. Zhu, Double-defect-induced polarization enhanced Ov-BiOBr/Cu$_{2−x}$S high-low junction for boosted photoelectrochemical hydrogen evolution, Appl. Catal. B Environ. 314 (2022) 121502.

[25] Y. Li, Q. Wu, Y. Chen, R. Zhang, C. Li, K. Zhang, M. Li, Y. Lin, D. Wang, X. Zou, T. Xie, Interface engineering Z-scheme Ti-Fe$_2$O$_3$/In$_2$O$_3$ photoanode for highly efficient photoelectrochemical water splitting, Appl. Catal. B Environ. 290 (2021), 120058.

[26] H.L. Ping Wang, Yanjie Cao, Huogen Yu, Carboxyl-functionalized graphene for highly efficient H$_2$-evolution activity of TiO$_2$ photocatalyst, Acta Phys. Chim. Sin. 37 (2021), 2008047.

[27] Z. Sun, H. Chen, L. Zhang, D. Lu, P. Du, Enhanced photocatalytic H$_2$ production on cadmium sulfide photocatalysts using nickel nitride as a novel cocatalyst, J. Mater. Chem. A 4 (2016) 13289–13295.

[28] L.H. Rongchen Shen, Qing Chen, Qiaoqing Zheng, Peng Zhang, Xin Li, P-Doped g-C$_3$N$_4$ nanosheets with highly dispersed Co$_{0.2}$Ni$_{1.6}$Fe$_{0.2}$P cocatalyst for efficient photocatalytic hydrogen evolution, Acta Phys. Chim. Sin. 38 (2022), 2110014.

[29] D. Jiang, L. Zhang, Q. Yue, T. Wang, Q. Huang, P. Du, Efficient suppression of surface charge recombination by CoP-Modified nanoporous BiVO$_4$ for photoelectrochemical water splitting, Int. J. Hydrog. Energy 46 (2021) 15517–15525.

[30] Z. Sun, M. Zhu, X. Lv, Y. Liu, C. Shi, Y. Dai, A. Wang, T. Majima, Insight into iron group transition metal phosphides (Fe$_2$P, Co$_2$P, Ni$_2$P) for improving photocatalytic hydrogen generation, Appl. Catal. B Environ. 246 (2019) 330–336.

[31] K. Li, K. Gong, J. Liu, Y. Yang, I. Nabi, A.U.R. Bacha, H. Cheng, J. Han, L. Zhang, New insights into the role of sulfite in BiOX photocatalytic pollutants elimination: In-operando generation of plasmonic Bi metal and oxygen vacancies, J. Hazard. Mater. 418 (2021), 126207.

[32] D. Zhang, H. Liu, C. Su, H. Li, Y. Geng, Combustion synthesis of highly efficient Bi/BiOBr visible light photocatalyst with synergetic effects of oxygen vacancies and surface plasma resonance, Sep. Purif. Technol. 218 (2019) 1–7.

[33] J. Li, Y. Yu, L. Zhang, Bismuth oxyhalide nanomaterials: layered structures meet photocatalysis, Nanoscale 6 (2014) 8473–8488.

[34] L. Ye, L. Zan, L. Tian, T. Peng, J. Zhang, The {001} facets-dependent high photoactivity of BiOCl nanosheets, Chem. Commun. 47 (2011) 6951–6953.

[35] P. Wen, K. Zhao, H. Li, J. Li, J. Li, Q. Ma, Scott M. Geyer, L. Jiang, Y. Qiu, In situ decorated Ni$_2$P nanocrystal cocatalysts on g-C$_3$N$_4$ for efficient and stable photocatalytic hydrogen evolution via a facile co-heating method, J. Mater. Chem. A 8 (2020) 2995–3004.

[36] J. Wang, X. Ma, F. Qu, A.M. Asiri, X. Sun, Fe-doped Ni$_2$P nanosheet array for high-efficiency electrochemical water oxidation, Inorg. Chem. 56 (2017) 1041–1044.

[37] Y. Dong, L. Kong, P. Jiang, G. Wang, N. Zhao, H. Zhang, B. Tang, A general strategy to fabricate Ni$_x$P as highly efficient cocatalyst via photoreduction deposition for hydrogen evolution, ACS Sustain. Chem. Eng. 5 (2017) 6845–6853.

[38] X. Li, J. Xiong, X. Gao, J. Ma, Z. Chen, B. Kang, J. Liu, H. Li, Z. Feng, J. Huang, Novel BP/BiOBr S-scheme nano-heterojunction for enhanced visible-light photocatalytic tetracycline removal and oxygen evolution activity, J. Hazard. Mater. 387 (2020) 121690.

[39] K. Maeda, K. Teramura, D. Lu, N. Saito, Y. Inoue, K. Domen, Noble-metal/Cr$_2$O$_3$ core/shell nano-particles as a cocatalyst for photocatalytic overall water splitting, Angew. Chem. Int. Ed. 45 (2006) 7806–7809.

[40] M.A. Mahadik, H. Chung, S. Lee, M. Cho, J.S. Jang, In-Situ noble fabrication of Bi$_2$S$_3$/BiVO$_4$ hybrid nanostructure through a photoelectrochemical transformation process for solar hydrogen production, ACS Sustain. Chem. Eng. 6 (2018) 12489–12501.

[41] P.E.A. Salomão, D.S. Gomes, E.J.C. Ferreira, F. Moura, L.L. Nascimento, A.O. T. Patrocínio, M.C. Pereira, Photoelectrochemical hydrogen production from water splitting using heterostructured nanowire arrays of Bi$_2$O$_3$/BiAl oxides as a photocathode, Sol. Energy Mater. Sol. Cells 194 (2019) 276–284.

[42] D. Cao, Q. Wang, Y. Wu, S. Zhu, Y. Jia, R. Wang, Solvothermal synthesis and enhanced photocatalytic hydrogen production of Bi/Bi$_2$MoO$_6$ co-sensitized TiO$_2$ nanotube arrays, Sep. Purif. Technol. 250 (2020) 117132.

[43] Y. Li, Y. Liu, Y. Hao, X.-j Wang, R.-h Liu, F.-t Li, Fabrication of core-shell BiVO$_4$@Fe$_2$O$_3$ heterojunctions for realizing photocatalytic hydrogen evolution via conduction band elevation, Mater. Des. 187 (2020), 108379.

[44] A.K. Vishwakarma, P. Tripathi, A. Srivastava, A.S.K. Sinha, O.N. Srivastava, Band gap engineering of Gd and Co doped BiFeO$_3$ and their application in hydrogen production through photoelectrochemical route, Int. J. Hydrog. Energy 42 (2017) 22677–22686.

[45] Y. Li, Q. Wang, X. Hu, Y. Meng, L. She, L. Wang, J. Huang, G. Zhu, Constructing NiFe-metal-organic frameworks from NiFe-layered double hydroxide as a highly efficient cocatalyst for BiVO$_4$ photoanode PEC water splitting, Chem. Eng. J. 433 (2022), 133592.

[46] J. Han, Y. Bian, X. Zheng, X. Sun, L. Zhang, A photoelectrochemical cell for pollutant degradation and simultaneous H$_2$ generation, Chin. Chem. Lett. 28 (2017) 2239–2243.

[47] Y. Jia, P. Liu, Q. Wang, Y. Wu, D. Cao, Q. Qiao, Construction of Bi$_2$S$_3$-BiOBr nanosheets on TiO$_2$ NTA as the effective photocatalysts: Pollutant removal, photoelectric conversion and hydrogen generation, J. Colloid Interface Sci. 585 (2021) 459–469.

[48] Z. Sun, H. Zheng, J. Li, P. Du, Extraordinarily efficient photocatalytic hydrogen evolution in water using semiconductor nanorods integrated with crystalline Ni$_2$P cocatalysts, Energy Environ. Sci. 8 (2015) 2668–2676.

[49] Y. Long, H. Xu, J. He, C. Li, M. Zhu, Piezoelectric polarization of BiOCl via capturing mechanical energy for catalytic H$_2$ evolution, Surf. Interfaces 31 (2022) 102056.

[50] J. Xiong, X. Li, J. Huang, X. Gao, Z. Chen, J. Liu, H. Li, B. Kang, W. Yao, Y. Zhu, CN/rGO@BPQDs high-low junctions with stretching spatial charge separation ability for photocatalytic degradation and H$_2$O$_2$ production, Appl. Catal. B Environ. 266 (2020), 118602.

[51] H. Tsuchiya, S. Fujimoto, T. Shibata, Semiconductive behavior of passive films formed on Fe-Cr alloy, J. Electroceram. 16 (2006) 49–54.

[52] L. Ai, L. Wang, M. Xu, S. Zhang, N. Guo, D. Jia, L. Jia, Defective Bi$_{.333}$(Bi$_6$S$_9$)Br/Bi$_2$S$_3$ heterostructure nanorods: Boosting the activity for efficient visible-light photocatalytic Cr(VI) reduction, Appl. Catal. B Environ. 284 (2021) 119730.

[53] D. Dai, L. Wang, N. Xiao, S. Li, H. Xu, S. Liu, B. Xu, D. Lv, Y. Gao, W. Song, L. Ge, J. Liu, In-situ synthesis of Ni$_2$P co-catalyst decorated Zn$_{0.5}$Cd$_{0.5}$S nanorods for high-quantum-yield photocatalytic hydrogen production under visible light irradiation, Appl. Catal. B Environ. 233 (2018) 194–201.